MATERIALS CHEMISTRY FRONTIERS

RESEARCH ARTICLE

View Article Online
View Journal | View Issue

Cite this: *Mater. Chem. Front.*, 2022, **6**, 2826

MOF-derived bimetallic core–shell catalyst HZSM-5@ZrO_2–In_2O_3: high CO_2 conversion in reverse water gas shift reaction†

Huimin Fang,[a] Guofeng Zhao, *[c] Denghui Cheng,[a] Jichang Liu, *[ab] Dengpeng Lan,[c] Qi Jiang,[a] Xuqiang Liu,[a] Jianping Ge,[c] Zhenliang Xu[a] and Haitao Xu *[a]

Received 6th April 2022,
Accepted 5th August 2022

DOI: 10.1039/d2qm00307d

rsc.li/frontiers-materials

The bicomponent core–shell catalyst HZSM-5@ZrO_2–In_2O_3 was synthesized *via* the decomposition of $In(NO_3)_3$/HZSM-5@UIO-66, which was obtained by impregnating HZSM-5@UIO-66 with $In(NO_3)_3$ solution. The bimetallic oxide particles of ZrO_2–In_2O_3 were formed through the simultaneous decomposition of UIO-66 and $In(NO_3)_3$, and were anchored to the surface of the HZSM-5 core. The HZSM-5@ZrO_2–In_2O_3 catalyst exhibited 31.1% CO_2 conversion with 96.3% CO selectivity at 400 °C for the reverse water gas shift reaction.

Introduction

With the rapid development of industry and increasing CO_2 emissions, the CO_2 concentration in the atmosphere has increased by 25% over the past 200 years, leading to severe environmental and ecological problems, such as the melting of glaciers, rising sea levels and climate change.[1] Thus, it is vital to utilize CO_2 to produce high-value-added fuels and chemicals for environmental improvement and industrial development. In recent years, green hydrogen has gradually become an economically and environmentally benign renewable energy,[2] and using it to reduce CO_2 is of great industrial value.[3] CO, CH_4 and CH_3OH are three major products from the direct utilization of CO_2. Among them, CO is widely used as a raw material for the further synthesis of alcohols,[4] olefins,[5] aromatics,[6] and other value-added chemicals. Therefore, the hydrogenation of CO_2 to CO is a promising way to reduce CO_2.[7]

Catalysts for the reverse water gas shift (RWGS) reaction are roughly divided into two categories, which are described as follows. Noble metal catalysts (such as Au,[8] Pt,[9] Pd,[10] *etc.*) have a high catalytic activity and stability, but they are very expensive and generate CH_4 as a non-negligible by-product; and non-noble metal catalysts (such as Fe,[11] Zn,[12] Ce,[13] *etc.*) are inexpensive but have a poor low-temperature activity. Hence many studies have focused on designing new catalysts to improve the catalytic performance of metals and oxides.[14] Indium oxide (In_2O_3) has attracted extensive attention due to its surface redox properties and excellent activity for CO_2 hydrogenation.[15–19] Abundant oxygen vacancies on the surface of In_2O_3 play an essential role in the activation of CO_2.[20,21] Since In_2O_3 is easily loaded and modified, other precious metals[22,23] or metal oxides[24,25] have often been introduced to form more oxygen vacancies and active sites, promoting the activation of CO_2 and H_2. However, most studies involving In_2O_3 have focused on the hydrogenation of CO_2 to methanol, and few studies have included the RWGS reaction.[26]

Metal–organic frameworks (MOFs) have wide applications in the field of catalysis[27–31] owing to their tunable composition and structure. Furthermore, MOF derivatives not only avoid the disadvantage of weak coordination bonds between metal clusters and organic linkers but also effectively inhibit metal oxide agglomeration in the pyrolysis process.[32] These factors are beneficial for fabricating stable catalysts with high dispersion, high specific surface area and high activity.[28]

Fig. 1 shows the typical assembly methods for catalysts. This work assembled the Zr-based MOF (UIO-66) and HZSM-5 *via* a solvothermal method to form a new composite HZSM-5@UIO-66. The HZSM-5@UIO-66 was impregnated with indium nitrate ($In(NO_3)_3$), followed by decomposition of the UIO-66 membrane and the adsorbed $In(NO_3)_3$ during calcination, resulting in the formation of the bicomponent core–shell catalyst HZSM-5@ZrO_2–In_2O_3. Due to the highly synergistic effect of the bimetal ZrO_2–In_2O_3 and the special core–shell structure of HZSM-5@ZrO_2–In_2O_3, the catalyst exhibited high

[a] *School of Chemical Engineering, East China University of Science and Technology, Shanghai, 200237, China. E-mail: xuhaitao@ecust.edu.cn*
[b] *Key Laboratory for Green Processing of Chemical Engineering of Xinjiang Bingtuan, School of Chemistry and Chemical Engineering, Shihezi University, Shihezi 832003, China. E-mail: liujc@ecust.edu.cn*
[c] *Shanghai Key Laboratory of Green Chemistry and Chemical Processes, School of Chemistry and Molecular Engineering, East China Normal University, Shanghai 200062, China. E-mail: gfzhao@chem.ecnu.edu.cn*

† Electronic supplementary information (ESI) available: Chemicals, general methods, characterization, procedures and additional figures. See DOI: https://doi.org/10.1039/d2qm00307d

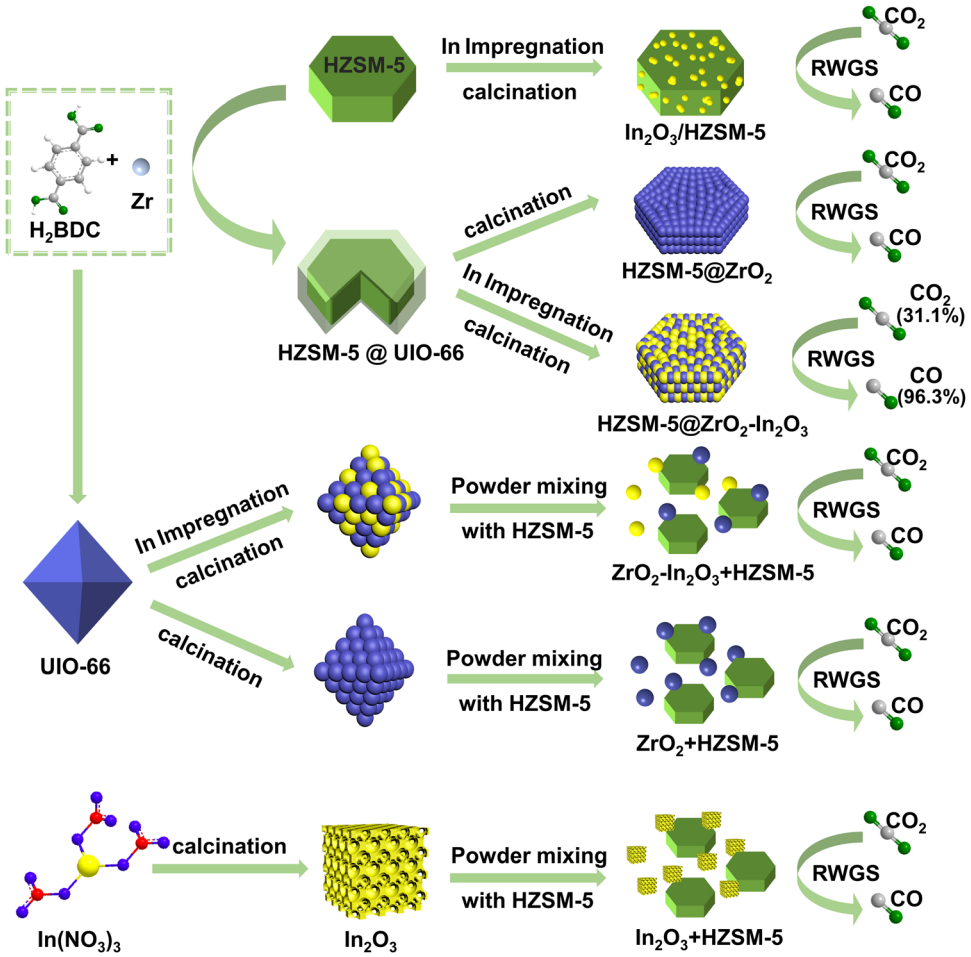

Fig. 1 Assembly diagram of composites (from top to bottom) In_2O_3/HZSM-5, HZSM-5@ZrO_2, HZSM-5@ZrO_2–In_2O_3, ZrO_2–In_2O_3 + HZSM-5, ZrO_2 + HZSM-5, In_2O_3 + HZSM-5 and their effects on CO_2 hydrogenation.

CO_2 conversion (31.1%) and excellent CO selectivity (96.3%) at 400 °C, 3 MPa, and 4500 mL g^{-1} h^{-1}.

Results and discussion

Syntheses and characterizations of fresh catalysts

HZSM-5 has been used widely in various catalytic reactions due to its regular pore channels, large surface area and thermal stability.[33,34] In Fig. 2, monodispersed HZSM-5[35] appears as smooth regular hexagonal prisms with a uniform size, while UIO-66[36] appears as octahedra. The HZSM-5 was placed in the UIO-66 precursor solution as a shape-directed carrier, and the UIO-66 was epitaxially grown onto the HZSM-5 core to obtain HZSM-5@UIO-66 *via* a solvothermal method. The morphology of the HZSM-5 core was well retained, while the UIO-66 was neither a regular octahedra nor small crystalline grains;[37] it was completely coated on HZSM-5 as a dense membrane layer (Fig. 2). The formation of the UIO-66 membrane can be attributed to the following factors. It has been confirmed that the solvent dipole moment can change the interfacial tension between the host nanoparticle and guest solvent, affecting the particle growth rate and ultimately changing the material morphology.[38] Thus, ethanol (EtOH, μ = 1.68 D) with a different dipole moment than *N*,*N*-dimethylformamide (DMF, μ = 3.86 D) was added to the preparation solution of the UIO-66 membrane. The optimal volume ratio of the two above-mentioned solvents was confirmed to be 1 : 1.[9,39] At this ratio, UIO-66 can grow uniformly along the epitaxial direction of the HZSM-5 core. In addition, the molar amounts of the metal sources (zirconium chloride ($ZrCl_4$)) and organic linkers (terephthalic acid (H_2BDC)) that constitute the UIO-66 had the most significant influence on the formation of the core–shell structure. The effect of $n(ZrCl_4)$ and $n(H_2BDC)$ on the growth of UIO-66 onto HZSM-5, under V_{EtOH}/V_{DMF} = 1 was investigated in this study. Fig. S2 (ESI†) shows the morphology of the UIO-66 grown on the HZSM-5 surface at different molar amounts. When $n(ZrCl_4)$ = $n(H_2BDC)$ = 0.035 mM, the UIO-66 membrane had a thickness of ~10 nm, and there were many standalone spherical UIO-66 crystals of about 40 nm in diameter. This result was ascribed to the high concentrations of the precursors in the solution, which promoted the growth of UIO-66 on the HZSM-5 surface, and led to the independent nucleation of UIO-66 crystals. To obtain a homogeneous material, $n(ZrCl_4)$ and $n(H_2BDC)$ were further reduced, from 0.035 mM to

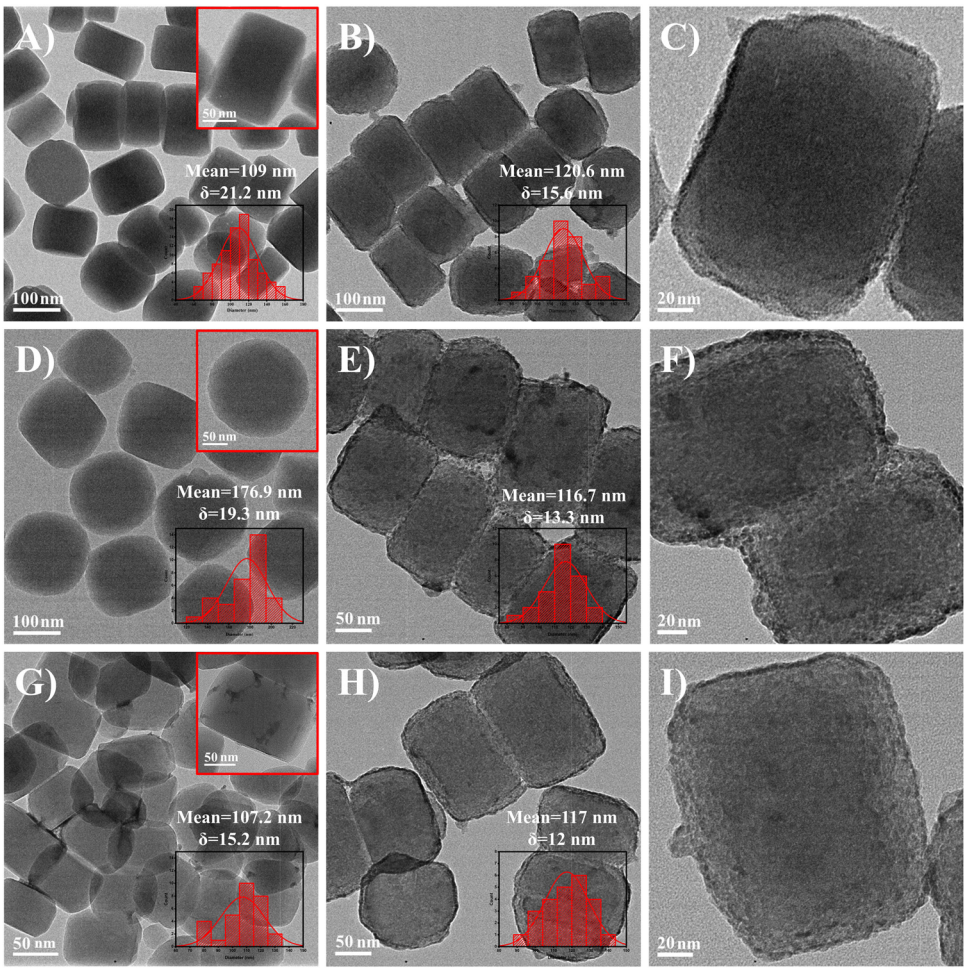

Fig. 2 TEM images of different materials: (A) HZSM-5, (B and C) HZSM-5@UIO-66, (D) UIO-66, (E and F) HZSM-5@ZrO_2–In_2O_3, (G) In_2O_3/HZSM-5, and (H and I) HZSM-5@ZrO_2.

0.025 mM, upon which both the UIO-66 membrane thickness and the standalone UIO-66 crystal size gradually decreased. Finally, when $n(ZrCl_4)$ and $n(H_2BDC)$ were reduced to 0.020 mM, there were almost no standalone UIO-66 particles, and the HZSM-5 surface was evenly covered by a 4 nm membrane. The enlarged view of HZSM-5@UIO-66 (Fig. 2C and Fig. S3D, ESI†) showed a continuous UIO-66 membrane around the periphery of HZSM-5. Therefore, 0.020 mM could be regarded as the optimal molar amount for the UIO-66 precursor. Furthermore, these results demonstrated that the UIO-66 membrane thickness in HZSM-5@UIO-66 could be effectively controlled by adjusting the precursor molar amounts.

HZSM-5@ZrO_2 and HZSM-5@ZrO_2–In_2O_3 (Fig. 2) originated from the calcination of HZSM-5@UIO-66 and $In(NO_3)_3$/HZSM-5@UIO-66, respectively. During calcination, the organic linkers (H_2BDC) in the UIO-66 membrane underwent oxidative decomposition with oxygen and, simultaneously, the UIO-66 membrane was converted to ZrO_2.[40] The disappearance of the organic linkers resulted in a certain volume contraction;[41,42] therefore, HZSM-5@ZrO_2 and HZSM-5@ZrO_2–In_2O_3 were slightly smaller in size than HZSM-5@UIO-66. The presence of organic linkers constructed a temporary physical barrier for the ZrO_2 nanoparticles, hindering their aggregation during calcination.[40] The metal oxides ZrO_2 and ZrO_2–In_2O_3 that were obtained after calcination were anchored on the HZSM-5 surface in the form of particles (Fig. 2F and I) about 5 nm in diameter. In the enlarged view (Fig. 2F and I and Fig. S3F, ESI†), the oxide shell on the surface of HZSM-5 can clearly be seen. Furthermore, compared with HZSM-5@ZrO_2–In_2O_3, only a small amount of In_2O_3 was loaded on the HZSM-5 (Fig. 2G) at the same In_2O_3 loading due to its worse adsorption than UIO-66. Clearly, coating UIO-66 on HZSM-5 could obtain ZrO_2–In_2O_3 with a small size and the catalyst with a higher In_2O_3 loading. Hollow cubes of pure In_2O_3, granular ZrO_2 and ZrO_2–In_2O_3 were also prepared (Fig. S4, ESI†).

The HAADF-STEM image of HZSM-5@UIO-66 (Fig. 3A) showed a large difference in brightness between the middle and edge regions of the material, indicating a typical core–shell structure. Energy-dispersive X-ray (EDX) elemental mapping and line-scan EDX (Fig. 3B–I) demonstrated the structural composition and elemental distribution of HZSM-5@UIO-66. Si and Al were the main components of the HZSM-5 core, and O existed in the whole material. Zr and C, which formed UIO-66, appeared as a shell, indicating that UIO-66 was successfully coated on the surface of the HZSM-5 core. Moreover, EDX

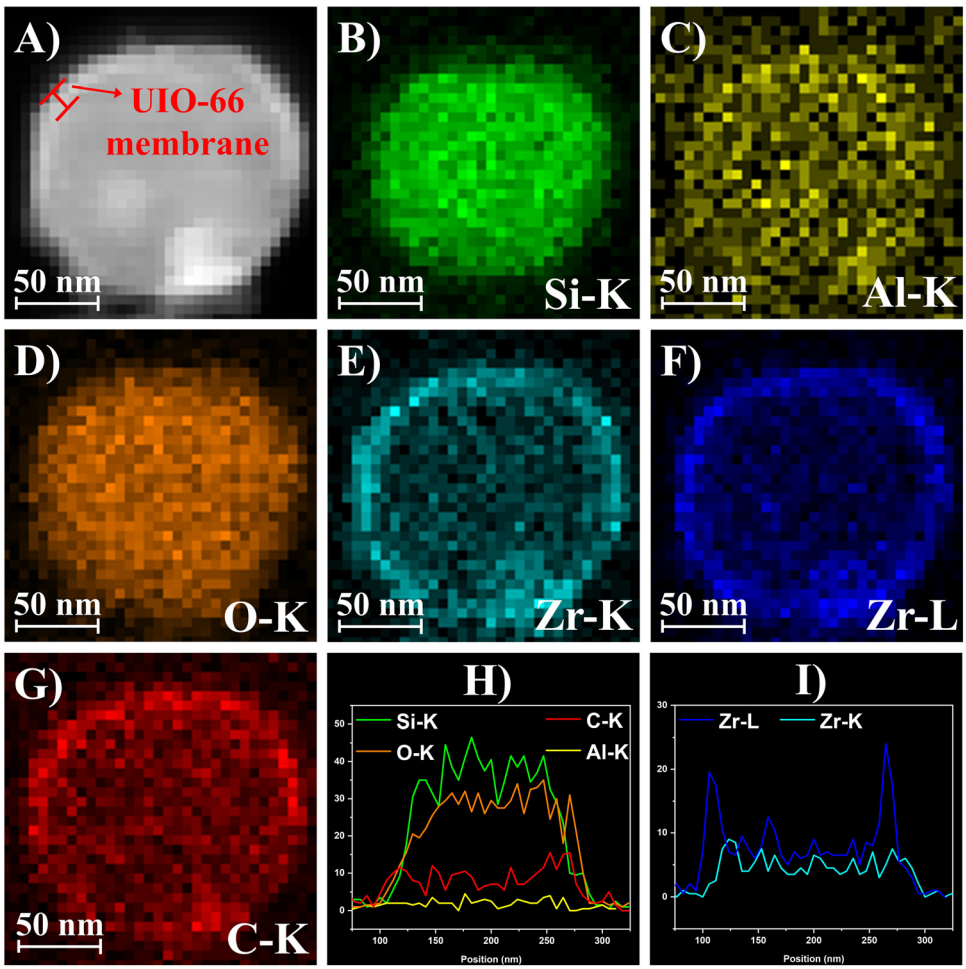

Fig. 3 (A) HAADF-STEM image of HZSM-5@UIO-66, (B–G) EDX elemental mapping of the selected region, and (H and I) line-scan EDX of HZSM-5@UIO-66.

elemental mapping (Fig. S5, ESI†) of HZSM-5@ZrO_2–In_2O_3 verified that In_2O_3 was successfully loaded on the surface of the material after impregnation.

The N_2 adsorption–desorption isotherms of UIO-66, HZSM-5, HZSM-5@UIO-66, and HZSM-5@ZrO_2–In_2O_3 were obtained (Fig. S6A, ESI†). All isotherms were the typical type-I, meaning that all the samples were microporous. However, the pore size distribution image (Fig. S6B, ESI†) of HZSM-5@ZrO_2–In_2O_3 showed the formation of mesopores. The disappearance of organic linkers in the UIO-66 membrane during calcination generated some extra spaces in the material, leading to mesopores.[40,43] The Brunauer–Emmett–Teller (BET) surface area of HZSM-5@UIO-66 was 296 $m^2\ g^{-1}$, which is lower than that of HZSM-5 (456 $m^2\ g^{-1}$), and significantly lower than that of UIO-66 (1307 $m^2\ g^{-1}$) (Table S1, ESI†). This is because HZSM-5 dominated the HZSM-5@UIO-66 composite, while the UIO-66 content was low. Furthermore, the UIO-66 membrane blocked part of the pores of HZSM-5 due to the mismatching aperture during preparation, which caused the BET surface area of HZSM-5@UIO-66 to be smaller than HZSM-5. HZSM-5@ZrO_2–In_2O_3 still maintained a high BET specific surface area (309 $m^2\ g^{-1}$).

Both UIO-66 and HZSM-5 showed diffraction peaks that matched their corresponding simulated powder X-ray diffraction (PXRD) patterns (Fig. S7, ESI†). However, for HZSM-5@UIO-66, only the characteristic peaks of HZSM-5 were observed. The absence of the characteristic peaks of UIO-66 might be attributed to its indistinguishability from HZSM-5 in the PXRD pattern and its low content in the composite. Although no UIO-66 diffraction peaks were observed in the PXRD pattern, Fourier transform infrared (FT-IR) spectroscopy (Fig. S9, ESI†) showed that both UIO-66 and HZSM-5@UIO-66 had the characteristic bands of UIO-66 at 1591, 1395 and 747 cm^{-1}, confirming the existence of the UIO-66 membrane in HZSM-5@UIO-66. HZSM-5@UIO-66 was calcined in air to obtain HZSM-5@ZrO_2, and its XRD pattern clearly showed the characteristic peaks of HZSM-5 and the highly crystalline tetragonal ZrO_2 (*t*-ZrO_2)[44] derived from the UIO-66 membrane. The peaks of HZSM-5 and pure cubic In_2O_3 (c-In_2O_3, formed *via* the pyrolysis of $In(NO_3)_3$)[45] were observed in In_2O_3/HZSM-5. By comparison with the precursors UIO-66 and HZSM-5@UIO-66, four new characteristic peaks (2θ = 25–70°) appeared in ZrO_2–In_2O_3 and HZSM-5@ZrO_2–In_2O_3. For ZrO_2–In_2O_3, the characteristic peaks of

UIO-66 disappeared completely due to the phase transition. The local spectra were magnified at 25–70° to verify the phase of the new peaks. For HZSM-5@ZrO_2–In_2O_3 (with an In_2O_3 loading of 20 wt%), only the diffraction peaks of *t*-ZrO_2 were observed because of impregnation loss and uniform distribution. When the In_2O_3 loading was increased to 70 wt%, the ZrO_2 peaks grew accordingly and shifted towards a higher diffraction angle (the characteristic peaks of ZrO_2–In_2O_3 (70 wt%) were the same as this), indicating that the loading was increased and some of the In_2O_3 was doped into ZrO_2.[46]

The peaks of In and Zr in HZSM-5@ZrO_2–In_2O_3 appeared at the corresponding positions of In^{3+} and Zr^{4+} (Fig. S10, ESI†), indicating the existence of oxides.[47] Compared with pure ZrO_2 and pure In_2O_3, new peaks appeared at higher binding energies. This phenomenon was ascribed to the change in the coordination states of In and Zr, which was caused by In doping in the ZrO_2 lattice to form the In–O–Zr structure (solid solution). This result was consistent with the XRD, and the In doping could force O ions away to balance the charge, forming more oxygen vacancies.[48] The O1s spectrum of HZSM-5@ZrO_2–In_2O_3 also exhibited a higher concentration of oxygen vacancies than HZSM-5@ZrO_2 (Fig. S10, ESI†).

Catalytic performance

For the prepared catalysts, three main products (CO, CH_4 and CH_3OH) were generated *via* the following three reactions. Since the appropriate reaction temperature for converting CO_2 to methanol was below 300 °C, only trace amounts of methanol were detected at 400 °C.

$$CO_2 + H_2 \rightleftharpoons CO + H_2O \quad \Delta H = 41.2 \text{ kJ mol}^{-1} \quad (1)$$

$$CO_2 + 4H_2 \rightleftharpoons CH_4 + H_2O \quad \Delta H = -164.9 \text{ kJ mol}^{-1} \quad (2)$$

$$CO_2 + 3H_2 \rightleftharpoons CH_3OH + H_2O \quad \Delta H = -49.4 \text{ kJ mol}^{-1} \quad (3)$$

In Fig. 4A, In_2O_3/HZSM-5 (where HZSM-5 was directly impregnated without coating with UIO-66) showed an inferior catalytic performance with 12.7% CO_2 conversion, and HZSM-5@ZrO_2 (where HZSM-5 was coated with UIO-66 but not impregnated) showed the lowest activity with 7.1% CO_2 conversion. However, HZSM-5@ZrO_2–In_2O_3 exhibited a superior CO_2 conversion (27.8%). On the one hand, the excellent adsorption and special pore structure of UIO-66 enabled HZSM-5@ZrO_2–In_2O_3 to have more active sites (Table S2, ESI†). On the other hand, the synergy of the ZrO_2–In_2O_3 bimetal played a crucial role in activating CO_2. To verify the improved catalytic performance of the bimetallic ZrO_2–In_2O_3 shell compared with the monometallic oxide, In_2O_3 + HZSM-5 and ZrO_2 + HZSM-5 were prepared (monometallic In_2O_3 and monometallic ZrO_2 were mixed with HZSM-5, respectively). The CO_2 conversion of HZSM-5@ZrO_2–In_2O_3 was about 2.5 and 3.4 times that of In_2O_3 + HZSM-5 and ZrO_2 + HZSM-5, respectively, suggesting a strong synergy between ZrO_2 and In_2O_3. The introduction of ZrO_2 can form the Zr–In interface and more oxygen vacancies,[49] significantly improving the adsorption and hydrogenation of CO_2.[50,51] In addition, materials with a core–shell structure have been shown to be superior catalysts in many reactions.[52] Hence for comparison, a mixed ZrO_2–In_2O_3 + HZSM-5 catalyst containing the same active oxide content as HZSM-5@ZrO_2–In_2O_3 was also prepared according to the ICP results (Table S2, ESI†). However, ZrO_2–In_2O_3 + HZSM-5 afforded a lower CO_2 conversion (22.6%) and CO yield (22.2%) than HZSM-5@ZrO_2–In_2O_3 (27.8%, 26.9%), suggesting that besides the same active sites, the core–shell structure of the HZSM-5@ZrO_2–In_2O_3 catalyst also plays an important role in this reaction. The physical mixing of ZrO_2–In_2O_3 and HZSM-5 was disordered, and the core–shell

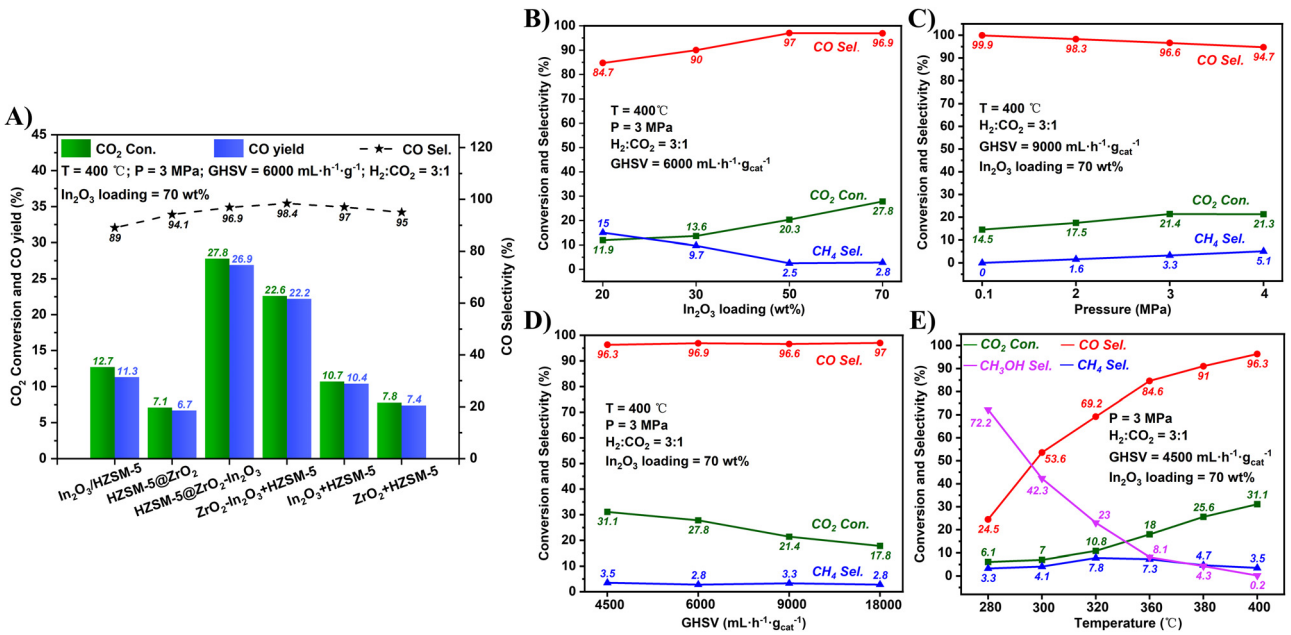

Fig. 4 Catalytic performance of (A) the various catalysts, (B) In_2O_3 loadings, (C) reaction pressures, (D) GHSV, and (E) reaction temperatures.

structure of ZrO_2–In_2O_3 and HZSM-5 improved the distribution of the ZrO_2–In_2O_3 components on the HZSM-5 surface. Although ZrO_2–In_2O_3 + HZSM-5 was not as active as HZSM-5@ZrO_2–In_2O_3, it still exhibited a higher CO_2 conversion and CO yield compared with the monometallic oxides (In_2O_3 + HZSM-5 and ZrO_2 + HZSM-5), which further proved the excellent catalytic performance of the MOF-derived bimetallic oxide in the RWGS reaction.

As shown in Fig. 4B, with the increase in In_2O_3 loading from 20 wt% to 70 wt%, the CO_2 conversion increased from 11.9% to 27.8%. The higher the In_2O_3 amount, the more the number of ZrO_2–In_2O_3 active sites. In addition, the operation conditions also have a significant influence on this reaction. Fig. 4C–E shows the influence of the pressure, space velocity (GHSV), and reaction temperature on the catalyst performance. When the pressure was 0.1 MPa, the CO_2 conversion was 14.5% with 99.9% CO selectivity. When the pressure was increased from 2 to 3 MPa, the CO_2 conversion increased from 17.5% to 21.4%. When the pressure was raised to 4 MPa, the CO_2 conversion hardly changed, but the CO selectivity decreased to 94.7%. The increase in pressure typically leads to increased collisions between the reactant gas molecules, activating more molecules, and promoting the adsorption of activated molecules on the catalyst surface, thereby increasing the CO_2 conversion. Moreover, the CO_2 methanation side-reaction has a reduced amount of gas molecules, and the high pressure tends to promote the side-reaction, thus decreasing the CO selectivity. With the GHSV increasing from 4500 to 18 000 mL h^{-1} $g_{cat}{}^{-1}$, the CO_2 conversion decreased from 31.1% to 17.8%, and the CO/CH_4 selectivity remained at around 97%/3%. The reduction in GHSV increased the residence time of the reactant gas in the catalyst bed, thus enhancing the CO_2 conversion. When the temperature was gradually increased from 280 to 400 °C, the CO_2 conversion increased from 6.1% to 31.1%. This is because CO_2 is inert and a high temperature is beneficial for activating CO_2. The CH_3OH selectivity decreased from 72% to 0.2% within this temperature range, while the CO selectivity increased from 24.5% to 96.3%. The RWGS reaction is a typical endothermic reaction, whereas the conversion of CO_2 to methanol is typically exothermic; hence increasing the temperature transforms the product from CH_3OH to CO. Based on the above discussions, the optimal reaction conditions for the HZSM-5@ZrO_2–In_2O_3 catalyst (In_2O_3 loading of 70 wt%) were as follows: 400 °C, 3 MPa, and 4500 mL h^{-1} $g_{cat}{}^{-1}$. Under these conditions, the CO_2 conversion and CO selectivity were 31.1% and 96.3%, respectively. Furthermore, only a small amount of methanol intermediate was generated due to the high reaction temperature, and the UIO-66 membrane might occupy the acidic sites of HZSM-5. Therefore, despite the presence of HZSM-5 in the catalysts, only very small amounts of hydrocarbons were detected in the product, while the main product was CO. Table S3 (ESI†) compares HZSM-5@ZrO_2–In_2O_3 with other catalysts, including metal oxides and noble metal catalysts, in the RWGS reaction. Both the CO_2 conversion and CO selectivity of HZSM-5@ZrO_2–In_2O_3 are outstanding. The special core–shell structure and the full synergistic effect of bimetallic ZrO_2–In_2O_3 play a critical role in enhancing the performance. In addition, compared with noble metal catalysts, In-based catalysts have lower costs and, thus, better practical application prospects in industries.

Catalytic mechanism

There are roughly two reaction mechanisms for the RWGS reaction, one of which is the redox mechanism.[53] In this process, H_2 does not directly participate in forming intermediates but acts only as a reducing agent to reduce the catalyst ($CO_2 + M^0 \rightarrow MO_x + CO$; $H_2 + MO_x \rightarrow M^0 + H_2O$). Since the main product with the HZSM-5@ZrO_2–In_2O_3 catalyst was CH_3OH at low temperature, the redox reaction was first excluded. The second most common mechanism is the degradation mechanism of the formate intermediate ($CO_2 \rightarrow$ *HCOO $\rightarrow$ CO* $\rightarrow$ CO).[54,55] In this pathway, H_2 is involved in the formation of the intermediate *HCOO. CO_2 is hydrogenated to the intermediate *HCOO on the catalyst surface, and the intermediate further decomposes to form CO. The combination of ZrO_2 and In_2O_3 increases the oxygen vacancies on the oxide surface, and the most significant role of the oxygen vacancies is in the adsorption and activation of CO_2.[21,56] Adsorbed CO_2 is further hydrogenated to the formate intermediate. This mechanism can explain the product transformation due to the change in temperature: formate is further hydrogenated to methanol at low temperature whereas it is directly pyrolyzed to CO at high temperature.

Conclusions

In conclusion, the bicomponent core–shell catalyst HZSM-5@ZrO_2–In_2O_3 was synthesized *via* the decomposition of $In(NO_3)_3$/HZSM-5@UIO-66, which was obtained by impregnating HZSM-5@UIO-66 with the $In(NO_3)_3$ solution. Under the synergistic effect of bimetallic ZrO_2–In_2O_3 derived from the UIO-66 membrane and $In(NO_3)_3$, the HZSM-5@ZrO_2–In_2O_3 catalyst with a special core–shell structure afforded excellent CO_2 conversion (31.1%) and CO selectivity (96.3%). The traditional concept is that the bimetallic oxide ZrO_2–In_2O_3 is suitable for CO_2 hydrogenation to methanol. This work reveals the superior catalytic performance of bimetallic ZrO_2–In_2O_3 derived from MOF towards the RWGS reaction, and provides a novel fabrication strategy for future catalysts for effectively catalysing CO_2 hydrogenation to CO.

Author contributions

Under Haitao Xu's guidance, Huimin Fang performed the experiments, collected and analyzed the data, then wrote the draft of the manuscript. Qi Jiang completed the XRD characterization, and the STEM characterization was completed by Dengpeng Lan. Denghui Cheng and Xuqiang Liu assisted in the experimental process. Haitao Xu and Guofeng Zhao revised the article. The manuscript was reviewed by Jichang Liu, Jianping Ge, and Zhenliang Xu. All the authors endorsed the final version of the manuscript.

Conflicts of interest

There are no conflicts to declare.

Acknowledgements

This work was supported by financial support from the Joint Fund by the National Natural Science Foundation of China and PetroChina (Project U1862204), the National Natural Science Foundation of China (No. 21371058 and No. 22179038) and the Special Project for Peak Carbon Dioxide Emissions-Carbon Neutrality (21DZ1206700) from the Shanghai Municipal Science and Technology Commission. The authors are grateful to the Research Center of Analysis and Testing, East China University of Science and Technology, and Prof. Jianping Ge from the Shanghai Key Laboratory of Green Chemistry of Chemical Processes, East China Normal University, for help in the transmission electron microscopy and high angle annular dark-field scanning transmission electron microscopy analysis.

Notes and references

1 J. Hansen, M. Sato, R. Ruedy, K. Lo, W. Lea David and M. Medina-Elizade, Global temperature change, *Proc. Natl. Acad. Sci. U. S. A.*, 2006, **103**, 14288–14293.

2 P. Lianos, Review of recent trends in photoelectrocatalytic conversion of solar energy to electricity and hydrogen, *Appl. Catal., B*, 2017, **210**, 235–254.

3 G. Centi, E. A. Quadrelli and S. Perathoner, Catalysis for CO_2 conversion: a key technology for rapid introduction of renewable energy in the value chain of chemical industries, *Energy Environ. Sci.*, 2013, **6**, 1711–1731.

4 B. Liu, Y. Li, Y. Duan, T. Ding, Y. Tang and C. Zheng, Effect of supports on performance of Cu–Fe based catalysts for higher alcohols synthesis from syngas, *React. Kinet., Mech. Catal.*, 2019, **128**, 695–706.

5 F. Jiao, J. Li, X. Pan, J. Xiao, H. Li, H. Ma, M. Wei, Y. Pan, Z. Zhou, M. Li, S. Miao, J. Li, Y. Zhu, D. Xiao, T. He, J. Yang, F. Qi, Q. Fu and X. Bao, Selective conversion of syngas to light olefins, *Science*, 2016, **351**, 1065–1068.

6 K. Cheng, W. Zhou, J. Kang, S. He, S. Shi, Q. Zhang, Y. Pan, W. Wen and Y. Wang, Bifunctional Catalysts for One-Step Conversion of Syngas into Aromatics with Excellent Selectivity and Stability, *Chem*, 2017, **3**, 334–347.

7 X. Zhang, X. Zhu, L. Lin, S. Yao, M. Zhang, X. Liu, X. Wang, Y.-W. Li, C. Shi and D. Ma, Highly Dispersed Copper over β-Mo_2C as an Efficient and Stable Catalyst for the Reverse Water Gas Shift (RWGS) Reaction, *ACS Catal.*, 2017, **7**, 912–918.

8 L. C. Wang, M. Tahvildar Khazaneh, D. Widmann and R. J. Behm, TAP reactor studies of the oxidizing capability of CO_2 on a Au/CeO_2 catalyst – A first step toward identifying a redox mechanism in the Reverse Water–Gas Shift reaction, *J. Catal.*, 2013, **302**, 20–30.

9 Y. Wu, D. Lan, J. Liu, J. Ge, H. Xu, Y. Han, H. Zhang, X. Pan, Z. Xu and J. Liu, UIO_{66}-membranized SAPO-34 Pt catalyst for enhanced carbon dioxide conversion efficiency, *Mater. Today, Energy*, 2021, **21**, 100781.

10 N. C. Nelson, L. Chen, D. Meira, L. Kovarik and J. Szanyi, In Situ Dispersion of Palladium on TiO_2 During Reverse Water–Gas Shift Reaction: Formation of Atomically Dispersed Palladium, *Angew. Chem., Int. Ed.*, 2020, **59**, 17657–17663.

11 D. H. Kim, S. W. Han, H. S. Yoon and Y. D. Kim, Reverse water gas shift reaction catalyzed by Fe nanoparticles with high catalytic activity and stability, *J. Ind. Eng. Chem.*, 2015, **23**, 67–71.

12 J. Wen, C. Huang, Y. Sun, L. Liang, Y. Zhang, Y. Zhang, M. Fu, J. Wu, L. Chen and D. Ye, The Study of Reverse Water Gas Shift Reaction Activity over Different Interfaces: The Design of Cu-Plate ZnO Model Catalysts, *Catalysts*, 2020, **10**(5), 533.

13 B. Dai, G. Zhou, S. Ge, H. Xie, Z. Jiao, G. Zhang and K. Xiong, CO_2 reverse water-gas shift reaction on mesoporous M-CeO_2 catalysts, *Can. J. Chem. Eng.*, 2017, **95**, 634–642.

14 Y. Xu, M. Cao and Q. Zhang, Recent advances and perspective on heterogeneous catalysis using metals and oxide nanocrystals, *Mater. Chem. Front.*, 2021, **5**, 151–222.

15 K. Sun, Z. Fan, J. Ye, J. Yan, Q. Ge, Y. Li, W. He, W. Yang and C.-J. Liu, Hydrogenation of CO_2 to methanol over In_2O_3 catalyst, *J. CO2 Util.*, 2015, **12**, 1–6.

16 P. Gao, S. Li, X. Bu, S. Dang, Z. Liu, H. Wang, L. Zhong, M. Qiu, C. Yang, J. Cai, W. Wei and Y. Sun, Direct conversion of CO_2 into liquid fuels with high selectivity over a bifunctional catalyst, *Nat. Chem.*, 2017, **9**, 1019–1024.

17 P. Gao, S. Dang, S. Li, X. Bu, Z. Liu, M. Qiu, C. Yang, H. Wang, L. Zhong, Y. Han, Q. Liu, W. Wei and Y. Sun, Direct Production of Lower Olefins from CO_2 Conversion via Bifunctional Catalysis, *ACS Catal.*, 2018, **8**, 571–578.

18 S. Wang, P. Wang, Z. Qin, W. Yan, M. Dong, J. Li, J. Wang and W. Fan, Enhancement of light olefin production in CO_2 hydrogenation over In_2O_3-based oxide and SAPO-34 composite, *J. Catal.*, 2020, **391**, 459–470.

19 S. Dang, P. Gao, Z. Liu, X. Chen, C. Yang, H. Wang, L. Zhong, S. Li and Y. Sun, Role of zirconium in direct CO_2 hydrogenation to lower olefins on oxide/zeolite bifunctional catalysts, *J. Catal.*, 2018, **364**, 382–393.

20 J. Ye, C. Liu, D. Mei and Q. Ge, Active Oxygen Vacancy Site for Methanol Synthesis from CO_2 Hydrogenation on In_2O_3(110): A DFT Study, *ACS Catal.*, 2013, **3**, 1296–1306.

21 J. Wang, G. Zhang, J. Zhu, X. Zhang, F. Ding, A. Zhang, X. Guo and C. Song, CO_2 Hydrogenation to Methanol over In_2O_3-Based Catalysts: From Mechanism to Catalyst Development, *ACS Catal.*, 2021, **11**, 1406–1423.

22 K. Sun, N. Rui, Z. Zhang, Z. Sun, Q. Ge and C.-J. Liu, A highly active Pt/In_2O_3 catalyst for CO_2 hydrogenation to methanol with enhanced stability, *Green Chem.*, 2020, **22**, 5059–5066.

23 N. H. M. D. Dostagir, C. Thompson, H. Kobayashi, A. M. Karim, A. Fukuoka and A. Shrotri, Rh promoted In_2O_3 as a highly active catalyst for CO_2 hydrogenation to methanol, *Catal. Sci. Technol.*, 2020, **10**, 8196–8202.

24 C. Y. Regalado Vera, N. Manavi, Z. Zhou, L.-C. Wang, W. Diao, S. Karakalos, B. Liu, K. J. Stowers, M. Zhou, H. Luo and D. Ding, Mechanistic understanding of support effect on the activity and selectivity of indium oxide catalysts for CO_2 hydrogenation, *Chem. Eng. J.*, 2021, **426**, 131767.
25 W. Wang, Y. Zhang, Z. Wang, J.-M. Yan, Q. Ge and C.-J. Liu, Reverse water gas shift over In_2O_3–CeO_2 catalysts, *Catal. Today*, 2016, **259**, 402–408.
26 Q. Sun, J. Ye, C.-J. Liu and Q. Ge, In_2O_3 as a promising catalyst for CO_2 utilization: A case study with reverse water gas shift over In_2O_3, *Greenhouse Gases: Sci. Technol.*, 2014, **4**, 140–144.
27 N. Martín, A. Portillo, A. Ateka, F. G. Cirujano, L. Oar-Arteta, A. T. Aguayo and M. Dusselier, MOF-derived/zeolite hybrid catalyst for the production of light olefins from CO_2, *ChemCatChem*, 2020, **12**, 5750–5758.
28 A. Pustovarenko, A. Dikhtiarenko, A. Bavykina, L. Gevers, A. Ramírez, A. Russkikh, S. Telalovic, A. Aguilar, J.-L. Hazemann, S. Ould-Chikh and J. Gascon, Metal–Organic Framework-Derived Synthesis of Cobalt Indium Catalysts for the Hydrogenation of CO_2 to Methanol, *ACS Catal.*, 2020, **10**, 5064–5076.
29 Z. Cai, J. Dai, W. Li, K. B. Tan, Z. Huang, G. Zhan, J. Huang and Q. Li, Pd Supported on MIL-68(In)-Derived In2O3 Nanotubes as Superior Catalysts to Boost CO_2 Hydrogenation to Methanol, *ACS Catal.*, 2020, **10**, 13275–13289.
30 Y. Wang, W. Zhan, Z. Chen, J. Chen, X. Li and Y. Li, Advanced 3D Hollow-Out ZnZrO@C Combined with Hierarchical Zeolite for Highly Active and Selective CO Hydrogenation to Aromatics, *ACS Catal.*, 2020, **10**, 7177–7187.
31 L.-L. Ling, W. Yang, P. Yan, M. Wang and H.-L. Jiang, Light-Assisted CO_2 Hydrogenation over Pd_3Cu@UiO-66 Promoted by Active Sites in Close Proximity, *Angew. Chem., Int. Ed.*, 2022, **61**, e202116396.
32 Y.-Z. Chen, R. Zhang, L. Jiao and H.-L. Jiang, Metal–organic framework-derived porous materials for catalysis, *Coord. Chem. Rev.*, 2018, **362**, 1–23.
33 Y. Yu, Z. Xi, B. Zhou, B. Jiang, Z. Liao, Y. Yang, J. Wang, Z. Huang, J. Sun and Y. Yang, Acidity Modification of ZSM-5 for Methane Conversion in Co-feeding Method with MTA Reaction, *Chem. Res. Chin. Univ.*, 2022, **38**, 1012–1017.
34 L. Luo, S. Wang, Z. Wu, Z. Qin, M. Dong, J. Wang and W. Fan, Influence of the ZSM-5 Support Acidity on the Catalytic Performance of Pd/ZSM-5 in Lean Methane Oxidation, *Chem. Res. Chin. Univ.*, 2022, **38**, 229–236.
35 Z. Wan, W. Wu, G. Li, C. Wang, H. Yang and D. Zhang, Effect of SiO_2/Al_2O_3 ratio on the performance of nanocrystal ZSM-5 zeolite catalysts in methanol to gasoline conversion, *Appl. Catal., A*, 2016, **523**, 312–320.
36 H. Xu, X. Luo, J. Wang, Y. Su, X. Zhao and Y. Li, Spherical Sandwich Au@Pd@UIO-67/Pt@UIO-n (n = 66, 67, 69) Core–Shell Catalysts: Zr-Based Metal–Organic Frameworks for Effectively Regulating the Reverse Water–Gas Shift Reaction, *ACS Appl. Mater. Interfaces*, 2019, **11**, 20291–20297.
37 G. Zhu, R. Graver, L. Emdadi, B. Liu, K. Y. Choi and D. Liu, Synthesis of zeolite@metal–organic framework core–shell particles as bifunctional catalysts, *RSC Adv.*, 2014, **4**, 30673–30676.
38 H. Bunzen, M. Grzywa, M. Hambach, S. Spirkl and D. Volkmer, From Micro to Nano: A Toolbox for Tuning Crystal Size and Morphology of Benzotriazolate-Based Metal–Organic Frameworks, *Cryst. Growth Des.*, 2016, **16**, 3190–3197.
39 X. Pan, H. Xu, X. Zhao and H. Zhang, Metal–Organic Framework-Membranized Bicomponent Core–Shell Catalyst HZSM-5@UIO-66-NH_2/Pd for CO_2 Selective Conversion, *ACS Sustainable Chem. Eng.*, 2020, **8**, 1087–1094.
40 J. Liu, Y. He, L. Yan, K. Li, C. Zhang, H. Xiang, X. Wen and Y. Li, Nano-sized ZrO_2 derived from metal–organic frameworks and their catalytic performance for aromatic synthesis from syngas, *Catal. Sci. Technol.*, 2019, **9**, 2982–2992.
41 G. Huang, F. Zhang, X. Du, J. Wang, D. Yin and L. Wang, Core–Shell $NiFe_2O_4$@TiO_2 Nanorods: An Anode Material with Enhanced Electrochemical Performance for Lithium-Ion Batteries, *Chem. – Eur. J.*, 2014, **20**, 11214–11219.
42 L. Zhang, H. B. Wu, S. Madhavi, H. H. Hng and X. W. Lou, Formation of Fe_2O_3 Microboxes with Hierarchical Shell Structures from Metal–Organic Frameworks and Their Lithium Storage Properties, *J. Am. Chem. Soc.*, 2012, **134**, 17388–17391.
43 G. Qu, P. Jia, T. Zhang, Z. Li, C. Chen and Y. Zhao, UiO-66(Zr)-derived t-zirconia with abundant lattice defect for remarkably enhanced arsenic removal, *Chemosphere*, 2022, **288**, 132594.
44 T. Numpilai, P. Kidkhunthod, C. K. Cheng, C. Wattanakit, M. Chareonpanich, J. Limtrakul and T. Witoon, CO_2 hydrogenation to methanol at high reaction temperatures over In_2O_3/ZrO_2 catalysts: Influence of calcination temperatures of ZrO_2 support, *Catal. Today*, 2021, **375**, 298–306.
45 J. Wang, C.-Y. Liu, T. P. Senftle, J. Zhu, G. Zhang, X. Guo and C. Song, Variation in the In_2O_3 Crystal Phase Alters Catalytic Performance toward the Reverse Water Gas Shift Reaction, *ACS Catal.*, 2020, **10**, 3264–3273.
46 C. Yang, C. Pei, R. Luo, S. Liu, Y. Wang, Z. Wang, Z.-J. Zhao and J. Gong, Strong Electronic Oxide–Support Interaction over In_2O_3/ZrO_2 for Highly Selective CO_2 Hydrogenation to Methanol, *J. Am. Chem. Soc.*, 2020, **142**, 19523–19531.
47 M. M. Zain, M. Mohammadi, N. Kamiuchi and A. R. Mohamed, Development of highly selective In_2O_3/ZrO_2 catalyst for hydrogenation of CO_2 to methanol: An insight into the catalyst preparation method, *Korean J. Chem. Eng.*, 2020, **37**, 1680–1689.
48 Z. Zhang, Y. Huang, H. Ma, W. Qian, H. Zhang and W. Ying, Syngas-to-olefins over MOF-derived ZnZrOx and SAPO-34 bifunctional catalysts, *Catal. Commun.*, 2021, **152**, 106292.
49 M. Zhang, M. Dou and Y. Yu, Theoretical study of the promotional effect of ZrO_2 on In_2O_3 catalyzed methanol synthesis from CO_2 hydrogenation, *Appl. Surf. Sci.*, 2018, **433**, 780–789.
50 M. Dou, M. Zhang, Y. Chen and Y. Yu, Mechanistic Insight into the Modification of the Surface Stability of In_2O_3

Catalyst Through Metal Oxide Doping, *Catal. Lett.*, 2018, **148**, 3723–3731.

51 O. Martin, A. J. Martín, C. Mondelli, S. Mitchell, T. F. Segawa, R. Hauert, C. Drouilly, D. Curulla-Ferré and J. Pérez-Ramírez, Indium Oxide as a Superior Catalyst for Methanol Synthesis by CO_2 Hydrogenation, *Angew. Chem., Int. Ed.*, 2016, **55**, 6261–6265.

52 Z. Wang, J. Qi, N. Yang, R. Yu and D. Wang, Core–shell nano/microstructures for heterogeneous tandem catalysis, *Mater. Chem. Front.*, 2021, **5**, 1126–1139.

53 G.-C. Wang and J. Nakamura, Structure Sensitivity for Forward and Reverse Water-Gas Shift Reactions on Copper Surfaces: A DFT Study, *J. Phys. Chem. Lett.*, 2010, **1**, 3053–3057.

54 C.-S. Chen, W.-H. Cheng and S.-S. Lin, Mechanism of CO formation in reverse water–gas shift reaction over Cu/Al_2O_3 catalyst, *Catal. Lett.*, 2000, **68**, 45–48.

55 A. M. Bahmanpour, M. Signorile and O. Kröcher, Recent progress in syngas production via catalytic CO_2 hydrogenation reaction, *Appl. Catal., B*, 2021, **295**, 120319.

56 Y. Zhang, L. Liang, Z. Chen, J. Wen, W. Zhong, S. Zou, M. Fu, L. Chen and D. Ye, Highly efficient Cu/CeO_2-hollow nanospheres catalyst for the reverse water-gas shift reaction: Investigation on the role of oxygen vacancies through in situ UV-Raman and DRIFTS, *Appl. Surf. Sci.*, 2020, **516**, 146035.

